

Understanding Electrolyte Filling of Lithium-Ion Battery Electrodes on the Pore Scale Using the Lattice Boltzmann Method

Martin P. Lautenschlaeger,^{*[a, b]} Benedikt Prifling,^[c] Benjamin Kellers,^[a, b] Julius Weinmiller,^[a, b] Timo Danner,^[a, b] Volker Schmidt,^[c] and Arnulf Latz^[a, b, d]

Electrolyte filling is a time-critical step during battery manufacturing that also affects battery performance. The underlying physical phenomena mainly occur on the pore scale and are hard to study experimentally. Therefore, here, the lattice Boltzmann method is used to study the filling of realistic 3D lithium-ion battery cathodes. Electrolyte flow through the nanoporous binder is modelled adequately. Besides process time, the influences of particle size, binder distribution, volume fraction and wetting behavior of active material and binder are

investigated. Optimized filling conditions are discussed by pressure-saturation relationships. It is shown how the influencing factors affect the electrolyte saturation. The amount and distribution of entrapped residual gas are analyzed in detail. Both can adversely affect the battery performance. The results indicate how the filling process, the final electrolyte saturation, and also the battery performance can be optimized by adapting process parameters as well as electrode and electrolyte design.

Introduction

Lithium-ion batteries are the major power source for battery electric vehicles. Its cell production is predicted to increase exponentially in the upcoming years. Therefore, the optimization of the battery production is key to reduce costs and the environmental impact of next-generation battery cells. Improving the battery manufacturing process requires the optimization of each process step. One of the process steps that has recently gained attention in this context, is the filling of cells with liquid electrolyte, where the electrolyte is first dosed into the cell and subsequently stored to achieve a uniform electrolyte distribution. Sometimes this procedure is even repeated to decrease entrapment of residual gas.^[1,2] Thus, the filling process is time-consuming and cost-intensive. It can take up to several days.^[1,3,4] Additionally, the filling also affects the battery performance and lifetime.^[3–6] It is known that poorly wetted

pores in electrodes cause the development of inhomogeneous solid electrolyte interphases (SEI).^[7] Moreover, they can lead to electrolyte decomposition during cycling,^[8] dendrite formation,^[1,5,9] and non-uniform current densities.^[4,10] An incomplete wetting can also have a large effect on the battery performance by increasing internal ionic resistances remarkably, which has recently been investigated for separators.^[11]

There are different strategies to prevent the aforementioned limitations and to increase the wettability and the final degree of electrode saturation. Either the filling process is sped up by cell evacuation and applying pressure gradients,^[1–5,12,13] applying elevated temperatures,^[14] or the physico-chemical properties of electrolyte and electrodes are tuned to improve the filling process.^[11] Two main approaches are considered in the literature. Electrolyte properties, i.e. surface tension and viscosity, are adjusted by electrolyte additives^[12,13,15] or the electrode wettability is improved using laser treatment,^[2,16] water-based electrode processing,^[17] or coatings and surfactants.^[6] Moreover, also structural properties of electrodes and separator are known to have a significant influence on the filling process.^[1,2,6,9,11,14,18] The compaction of the electrode by calendering, e.g., increases the filling duration and the amount of residual gas.^[1,2,6,14,18]

Recently, different experimental studies have investigated the filling process using in-situ methods. Amongst those were electrochemical impedance spectroscopy,^[13,19] neutron radiography,^[2–4,13] X-ray measurements,^[9] focused ion beam combined with scanning electron microscopy,^[18] thermography,^[6] and wetting balance tests.^[6] However, most of those methods are complex and time-consuming. They all suffer from low spatial or temporal resolution, imprecise localization of the wetting front, or cannot resolve the interdependency of the different influencing factors. Thus, a comprehensive understanding especially of pore-scale phe-

[a] Dr. M. P. Lautenschlaeger, B. Kellers, J. Weinmiller, Dr. T. Danner, Prof. A. Latz
German Aerospace Center (DLR), Institute of Engineering Thermodynamics, 70569 Stuttgart, Germany
E-mail: martin.lautenschlaeger@dlr.de

[b] Dr. M. P. Lautenschlaeger, B. Kellers, J. Weinmiller, Dr. T. Danner, Prof. A. Latz
Helmholtz Institute Ulm for Electrochemical Energy Storage (HIU), 89081 Ulm, Germany

[c] B. Prifling, Prof. V. Schmidt
Ulm University (UULM), Institute of Stochastics, 89081 Ulm, Germany

[d] Prof. A. Latz
Ulm University (UULM), Institute of Electrochemistry, 89081 Ulm, Germany

 Supporting Information for this article is available on the WWW under https://doi.org/10.1002/batt.202200090

 © 2022 The Authors. *Batteries & Supercaps* published by Wiley-VCH GmbH. This is an open access article under the terms of the Creative Commons Attribution Non-Commercial License, which permits use, distribution and reproduction in any medium, provided the original work is properly cited and is not used for commercial purposes.

nomena during the filling process is missing.^[18] There is still no common agreement on how to optimize this process, especially for the multitude of electrochemical systems and cell types available on the market.^[5]

A method that is capable of giving a detailed insight into the wetting phenomena and the interdependency of the influencing factors are direct numerical simulations in general, and the lattice Boltzmann method (LBM) in particular. LBM has proven to be a reliable tool for the simulation of transport processes and fluid flow.^[20,21] In contrast to conventional fluid dynamics, it gives access to multi-scale and multi-physics issues even within complex geometries, e.g., in porous media.^[22,23]

The multi-component Shan-Chen pseudopotential method (MCSC) has regularly been utilized to simulate multi-phase flows with LBM.^[22–24] Similar to molecular dynamics simulations, where molecular interactions are modeled to study, e.g., wetting phenomena^[25–27] or transport processes,^[28,29] it uses fluid-fluid and solid-fluid interaction forces to model interfacial tension and adhesion forces, respectively.^[23]

So far, LBM has been successfully applied to investigate water transport and hysteresis effects in catalyst or gas diffusion layers of polymer electrolyte membrane fuel cells.^[30–36] However, it has rarely been applied in the context of battery simulations.^[37–40] Only a few studies have been conducted in which LBM was applied to study electrolyte filling processes.^[41–44] Jeon and co-workers^[41–43] as well as Mohammadian and Zhang^[45] studied the effect of structural properties and wettability on the filling duration. However, the underlying microstructures of the electrodes were rather simplified. Moreover, only 2D simulations were conducted, although this reduces the number of flow paths significantly and thereby strongly affects the saturation behavior, pore blocking, gas entrapment, and the simulation accuracy.^[38,43] Electrolyte filling of realistic 3D lithium-ion battery electrodes using LBM was investigated only recently by Shodiev *et al.*^[44,46] Their studies focused on the correlation between the structural properties of electrodes and the filling duration, from which the data were also used to train a machine learning algorithm. However, the wetting properties of active material and binder were assumed to be equal and the binder was fully solid and impermeable without considering its nanoporosity.

The present paper extends the findings of the aforementioned studies.^[44,46] In particular, the electrolyte filling process of realistic virtual 3D lithium-ion battery electrode structures is studied using LBM. The simulation setups and boundary conditions that are used mimic experimental setups. In addition, electrode structures and LBM model parameters are chosen such that they represent authentic materials typically used for lithium-ion batteries. Furthermore, motivated by the work of Pereira,^[47–49] MCSC is combined with a homogenization approach that is based on the grayscale (GS) or partial bounce-back (PBB) method.^[50] This allows to simultaneously study the electrolyte flow in the mesoscopic pores confined by active material particles as well as in the nanoscopic pores of the binder without structurally resolving the latter. Note that our model is applied to simulate electrolyte wetting in lithium-ion battery cathodes, but is not limited to this particular applica-

tion. Other research fields can benefit from this development, e.g., flow phenomena in redox-flow batteries and fuel cells. Using our model, the process time as well as the influence of a wide range of relevant structural and physico-chemical properties of lithium-ion battery cathodes are studied. More precisely, the influence of the particle size distribution R_{PS} , the volume fraction ϕ_A , and the wettability θ_A of the active material on the filling process is investigated. In addition, a permeable binder is virtually added to some of the electrodes for which the inner volume fraction ϕ'_B and the wettability θ_B are varied.

This study aims to increase the understanding of the electrolyte filling process on the pore scale. It gives insight into the sensitivity of the aforementioned parameters on pressure-saturation behavior during filling and electrolyte saturation. For each electrode customized pressure profiles are determined that ensure a steady and uniform filling process. Finally, the amount and the size distribution of entrapped residual gas agglomerates are analyzed in detail. It is shown how the residual gas phase can adversely affect the battery performance. Moreover, permeabilities are determined to estimate the efforts for displacing gas agglomerates from the electrodes in a subsequent production step. All in all, the results presented here are helpful to optimize electrode and electrolyte design as well as the filling process. The findings are also applicable to optimize the filling of anodes, separators or other battery types.

The present paper is organized as follows. The simulation setup is given in Section "Simulation Setup", where also the electrode structure generation and the analysis are described. Section "Overview of the Study" gives an overview of the study including the influencing factors. The results are presented and discussed in Section "Results and Discussion". Finally, conclusions are drawn in Section "Conclusion".

Simulation Setup

Artificially generated 3D lithium-ion battery cathode structures^[51] were used as a geometrical basis for all simulations. Some structures were additionally infiltrated with binder using a physically motivated algorithm as described in.^[52] The electrolyte properties were chosen to represent propylene carbonate. The LBM model that was used for all simulations as well as its parametrization are described in detail in the Supporting Information (cf. Section S1 and Table S1). All simulations have been carried out with an extended version of the open-source LBM tool *Palabos* (version 2.3).^[53]

Recall that the focus of the present paper is twofold. First, the pressure-saturation behavior during the filling is studied. It shows optimum pressure profiles that ensure a steady and uniform filling process. Second, the systems obtained at the end of the filling are analyzed. The analysis concerns the final electrolyte saturation, the size and spatial distribution of gas agglomerates being entrapped, and the permeability of electrolyte and gas in those partially saturated electrodes. Moreover, it is shown how an imperfect filling might affect the battery performance.

Artificial Generation of Electrode Structures

The underlying cathode structures have been generated by means of the stochastic microstructure modeling framework which is described in [51]. It consists of three steps. First, a force-biased collective rearrangement algorithm is used to model positions and sizes of active particles by a non-overlapping sphere packing.^[54,55] The packing density corresponds to the predefined volume fraction of active material and is varied in the range $\phi_A = \{0.5, 0.6, 0.7\}$ to obtain different electrode densities. Note that the radii of the spheres are drawn from a Gamma distribution, denoted by R_{PS} , with some shape and rate parameters $\alpha, \beta > 0$. The following three cases are considered: Small spheres ($\alpha = 3.94, \beta = 2.17 \mu\text{m}^{-1}$), medium spheres ($\alpha = 2.62, \beta = 1.05 \mu\text{m}^{-1}$), and large spheres ($\alpha = 2.65, \beta = 0.75 \mu\text{m}^{-1}$). The second modeling step involves a connectivity graph^[51] which is omitted here due to the high volume fractions of active material. The shape of the simulated particles follows the distribution of particle shapes that is also observed in realistic electrode structures. Thus, in the third step, each sphere was replaced by a not necessarily spherical particle, i.e. a structural anisotropy is introduced which is small enough such that simulation results are only affected within the uncertainty of the method (cf. Section S3). Particle sizes and shapes are described by means of a radius function. This function is represented by a truncated series expansion in terms of spherical harmonics,^[56] with the truncation parameter $L = 6$. The simulation of active particles represented in this way was carried out by means of Gaussian random fields on the sphere. The corresponding angular power spectrum is given by $a_1 = 0.65, a_2 = 4.13, a_3 = 0.82, a_4 = 0.31, a_5 = 0.17, a_6 = 0.11$ (cf. [57] for details).

Finally, the system of simulated particles was discretized using a voxel size of $0.438 \mu\text{m}$. In dependence on the volume fraction $\phi_A = \{0.5, 0.6, 0.7\}$, the number of voxels was 82, 170,

and {388, 323, 277} along the x -, y -, and z -direction, respectively. Note that periodic boundary conditions in y - and z -direction were applied in all simulations. For the simulation scenarios with the IDs 9–14, a volume fraction of $\phi_B = 0.21$ of the binder was added to the reference structure, i.e. ID 1 (cf. Table 1). Therefore, a morphological closing of the active material was applied where a sphere was used as the structuring element.^[58] The radius of the sphere was chosen such that the predefined volume fraction of the binder was obtained.

Pressure-Saturation Behavior

The relationship between capillary pressure and saturation is an important measure for porous media applications. It is used to predict which capillary pressure has to be overcome to reach a certain saturation.^[59,60] Our simulation setup mimics experimental setups that are typically used to determine capillary pressure-saturation curves of porous media, e.g., in the context of fuel cells.^[61–64] A scheme of the simulation setup that was used to study the pressure-saturation behavior is shown in Figure 1. It consists of the electrode structure as described in the previous section. The total pore space, i.e. the unification of the mesoscopic pores confined by the active material and the inner pores in the binder, was initially filled with a gas of density ρ^G and the dissolved electrolyte with density ρ_{dis}^E .

Large scale simulations have been conducted. For $\phi_A = \{0.5, 0.6, 0.7\}$, the system sizes were $40 \mu\text{m}, 75 \mu\text{m}$, and $\{170, 140, 120\} \mu\text{m}$ along the x -, y -, and z -direction, respectively. This corresponds to simulation domains of up to 5.9 million lattice cells. The simulations were computationally expensive and, thus, conducted on the supercomputers JUSTUS 2 and Hawk using more than 500 cores in parallel execution.

Table 1. Simulation overview. The default simulation without binder is ID 1. The default simulation with binder is ID 9, where the properties of the active material were identical to those of ID 1. The simulations 1–8, 15, and 16 did not contain binder and thus are marked by ‘–’ in columns 5 and 6. In contrast, the simulations 9–14 contained binder. Plain entries of settings have the same value as ID 1 or ID 9, respectively. Beside the total duration of the filling process t_{end} , also the final saturation $S_{final}^E = S^E(t_{end})$, as well as the permeability of the electrolyte k_y^E and the residual gas phase k_y^G are given.

sim. ID	R_{PS}	ϕ_A	θ_A [°]	ϕ'_B	θ_B [°]	t_{end} [10^{-2} s]	S_{final}^E [%]	k_y^E [10^{-15} m^2]	k_y^G [10^{-15} m^2]
1	medium	0.6	90	–	–	1.46	89.6	91.72	9.62
2	small	–	–	–	–	1.41	90.7	102.58	10.55
3	large	–	–	–	–	1.52	95.3	198.66	70.64
4	–	0.7	–	–	–	1.26	79.1	32.28	5.82
5	–	0.5	–	–	–	1.48	95.6	264.33	97.59
6	–	–	60	–	–	1.48	96.8	88.98	40.97
7	–	–	80	–	–	1.48	92.7	92.16	16.38
8	–	–	100	–	–	1.42	86.1	91.64	9.66
9	medium	0.6	90	0.5	60	1.39	95.9	9.82	1.00
10	–	–	–	0.6	–	1.39	95.5	7.21	1.06
11	–	–	–	0.4	–	1.38	95.3	13.19	1.64
12	–	–	–	–	30	1.35	96.6	10.03	5.93
13	–	–	–	–	90	1.35	89.1	8.80	1.75
14	–	–	–	–	120	1.02	63.0	4.99	1.89
15	medium	0.6	90	–	–	2.98	90.1	92.21	8.11
16	medium	0.6	90	–	–	0.73	89.3	91.30	10.63

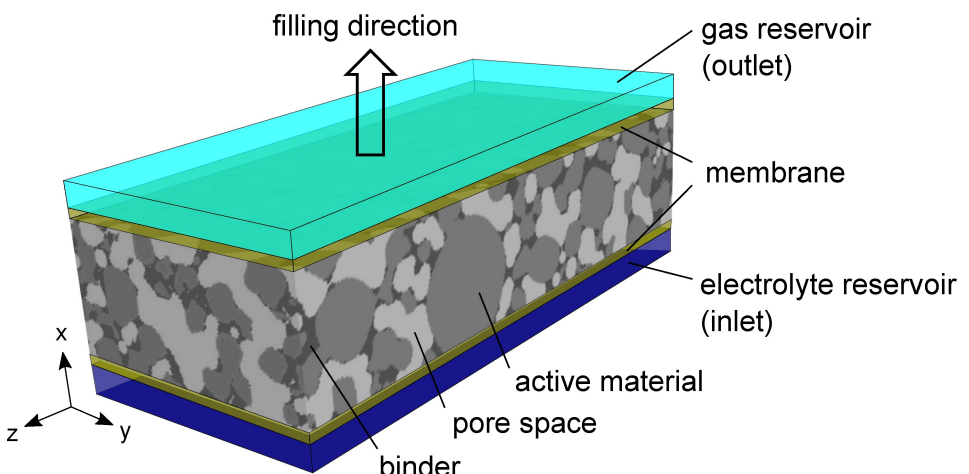


Figure 1. Scheme of the simulation setup. The electrode consists of active material (gray) and potentially a binder (darker gray) both enclosing the mesoscopic pore space (lighter gray). The reservoirs in which the densities of electrolyte and gas were prescribed are marked in blue and cyan, respectively. The membranes adjacent to the reservoirs are depicted in yellow. They were semi-permeable during the electrolyte filling process in +x-direction and impermeable during the permeability simulations in which a driving force was applied in +y-direction.

In the present study, only filling in x-direction was investigated. From preliminary studies and the literature,^[14] this is assumed to have no systematic influence on the results, as the electrodes were almost isotropic. Periodic boundary conditions were applied along the y- and z-direction. Along the x-direction an electrolyte reservoir and a gas reservoir were added at the inlet and outlet, respectively. The reservoirs had a thickness of four layers each. They were used to prescribe the density of the corresponding fluid, i.e. proportional to the pressure (cf. Eq. (S15)). The initial electrolyte density at the inlet was ρ^E (and the gas density to ρ_{dis}^G). During the simulation run, ρ^E at the inlet was incrementally increased using a control loop under the condition of steady and uniform filling with a predefined target saturation rate. The gas density at the outlet was constant, i.e. ρ^G (and the electrolyte density at ρ_{dis}^E). Thereby, a pressure difference between the two fluid phases is applied that corresponds to the capillary pressure (cf. Eq. (1)). This approach is in accordance with experiments and simulations, where the capillary pressure is adjusted by increasing or decreasing the pressure of the wetting phase or the nonwetting phase, respectively.^[31,33,35,61–64] Each reservoir was divided from the electrode by a semi-permeable membrane to prevent an unwanted fluid breakthrough. The inlet membrane was permeable for the electrolyte only. The outlet membrane was permeable for the gas only. The impermeability was implemented by applying the bounce-back scheme (cf. [21]) to the non-permeating fluid.

From the simulations the pressure difference Δp was determined as

$$\Delta p = \langle p \rangle_{\text{inlet}} - \langle p \rangle_{\text{outlet}}, \quad (1)$$

where p was evaluated using Eq. (S15), and $\langle p \rangle$ denotes the average pressure in the inlet and outlet reservoirs. The pressure difference Δp is directly related to the capillary pressure p_c as $p_c = p_0 - \Delta p$, where p_0 is the absolute capillary pressure at zero

electrolyte saturation ($p_0 = p_c(S^E = 0)$). In the current work, Δp was chosen over p_c to improve the comparability and ensure that all pressure-saturation curves start from the same value $\Delta p(S^E = 0) = 0$.

The electrolyte saturation S^E is defined as

$$S^E = \frac{N_{\text{pore}}(\rho^E \geq 0.5) + (1 - n_s)N_{\text{binder}}(\rho^E \geq 0.5)}{N_{\text{pore}} + (1 - n_s)N_{\text{binder}}}, \quad (2)$$

where the denominator and numerator correspond to the total pore space and the pore space in which $\rho^E \geq 0.5 \text{ mlu}^{-3}$, respectively. The number of pore lattice cells in the electrode structures and the binder are denoted by N_{pore} and N_{binder} , respectively. The latter are multiplied by the effective nanoscopic pore volume $(1 - n_s) = (1 - \phi_b)$. Note, that for the calculation of the saturation only the lattice cells between the two membranes were considered.

A simulation run consisted of approximately 1,000,000 time steps. Only the two simulations in which the process time was varied by the factor 0.5 and 2, accordingly consisted of approximately 500,000 and 2,000,000 time steps. The pressure difference and the saturation were determined every 10,000 time steps during the production run. The simulations were stopped when a further saturation was not possible and led to a steep increase of Δp . The corresponding distribution functions of both fluids were used for further data analysis and as input for subsequent permeability simulations.

The statistical uncertainty of the pressure-saturation curves was estimated for a representative electrode structure. The mean standard deviation of the average curve was 2–4 kPa for Δp and to 0.75% for S^E . Detailed results are given in the Supporting Information (cf. Section S3).

Gas Entrapment

As was recently reported by Sauter *et al.*,^[11] gas entrapment can significantly reduce effective ionic conductivities in separators. The gas phase is a poor conductor that hinders ion transport, blocks transport pathways, and reduces the connectivity of the electrolyte phase. This can be quantified by the mean geodesic tortuosity.^[65,66] It is determined by the lengths of shortest paths between inlet and outlet plane completely contained in a predefined phase. In this study, it is computed using Dijkstra's algorithm.^[67] Dividing the lengths of those shortest paths by the thickness of the electrode in *x*-direction and subsequently averaging over all starting points in the inlet, an estimator of the mean geodesic tortuosity is obtained.^[68]

Two different geodesic tortuosities are determined, i.e. τ_0 and τ_{end} . For τ_0 , the active material and partially also the binder are considered as obstacles for the ionic transport. Thus, τ_0 represents the geodesic tortuosity for an ideal case in which each pore contributes to the ionic pathways. In contrast, τ_{end} is the geodesic tortuosity at the end of the filling process. Then, also entrapped gas is an obstacle for densities exceeding $\rho^G \geq 0.5$. In case of simulations with binder (IDs 9–14), an additional weighting factor w_B accounts for increased path lengths within a binder.^[69] More precisely, the equation $w_B = \phi_B'^{-0.5}$ is used, which corresponds to the Bruggeman relation^[70] and the frequently used Bruggeman exponent of -0.5 .^[71,72]

In addition, gas that accumulates at the surface of active material reduces the electrochemically active surface area and, thereby, limits the lithiation process. Thus, blocked surface areas of active material are analyzed. For this purpose, the surface area of active material (S_A), gas (S_G) and the union of both (S_{AUG}) is estimated from voxelized image data by means of differently weighted local $2 \times 2 \times 2$ voxel configurations, using the weights proposed in [73]. Thereby, the fraction S_{AUG} of blocked active material surface is determined as

$$S_{\text{AUG}} = \frac{S_A + S_G - S_{\text{AUG}}}{2S_A} \in [0, 1]. \quad (3)$$

Note that the interfacial area between active material and gas contributes to S_A and S_G but not to S_{AUG} , which leads to the factor of 2 in the denominator.

Permeability

The permeability k is a measure for the ability of a porous medium to perfuse fluid flow. Thus, it represents fluid mobility. In this study, the permeability is used to quantify the effort that is necessary for displacing entrapped gas agglomerates from electrodes.

The simulation setup for determining the permeability is similar to the setup in the previous section. Only deviations from this setup are described here. Electrolyte and gas distributions were initialized identical to those at the end of the filling process. Periodic boundary conditions were applied

along all directions. The membranes were fully impermeable to conserve the fluid composition within the electrode. The densities of both fluids were constant. Along the positive *y*-direction the external force density $f_y = 5 \cdot 10^{-4} \text{ luts}^{-2}$ was applied. It was chosen such that the momentum showed a linear relationship with the external force.^[74–76] The permeabilities were determined between the two membranes only.

From the simulations the permeability k_y^σ of the component σ along the *y*-direction was determined as

$$k_y^\sigma = \frac{u_{\text{Darcy},y}^\sigma \nu^\sigma}{f_y}. \quad (4)$$

Thus, k_y^E and k_y^G denote the permeabilities of the electrolyte and the residual gas phase, respectively. While ν and f_y were input parameters to the simulations, the Darcy velocity $u_{\text{Darcy},y}^\sigma$ of the σ -component in *y*-direction was determined from the simulations as

$$u_{\text{Darcy},y}^\sigma = \frac{\sum_j^{N_{\sigma,\text{bulk}}} u_y^\sigma(x_j)}{N_{\text{total}}}. \quad (5)$$

The Darcy velocity is the sum of the velocity component in the *y*-direction, u_y , over all lattice cells $j \in N_{\sigma,\text{bulk}}$ that belong to the bulk phase of the σ -component $N_{\sigma,\text{bulk}}$, divided by the total number of lattice cells N_{total} . The bulk phase did only contain fluid lattice cells without direct contact to a solid and in which the dissolved density of the complementary $\bar{\sigma}$ -component, $\rho_{\text{dis}}^{\bar{\sigma}}$, was below 0.2 mlu^{-3} to reduce errors from spurious currents.^[22,77]

Each simulation consisted of two parts. Initially 100,000 time steps were performed in which a steady state was established. Subsequently, a production run of 100,000 time steps was conducted during which the permeability was determined every 1,000 time steps.

Overview of the Study

The influencing factors on the electrolyte filling process that are considered are: the filling speed or process time t_p , the particle size distribution R_{PS} , the volume fraction ϕ_A , and the wettability θ_A of active material, as well as the inner volume fraction ϕ'_B and wettability θ_B of binder. The volume fraction ϕ_A is the number of active material lattice cells divided by the total number of lattice cells. In contrast, the inner volume fraction ϕ'_B is the volume fraction of solid binder within a single binder lattice cell. Here it was assumed that $\phi'_B = n_s$, which is a simplification and not generally true.^[49,50]

An overview of the simulations from the current work is given in Table 1. To determine the pressure-saturation behavior, 16 large-scale 3D simulations were conducted. Another 16 simulations were conducted to determine permeabilities. The material properties of active material (IDs 1–8) and binder (IDs 9–14) were varied in a range that represents relevant electrode structures. The contact angles of propylene carbonate on the active material ($\theta_A = [60, 100]^\circ$) and the binder ($\theta_B = [30, 120]^\circ$)

were chosen in a range that was observed in experiments.^[11,12,78–80] Note that for other electrolyte-electrode combinations also lower contact angles might be relevant (cf. [11, 12, 14, 78]). For all aforementioned simulations, i.e. IDs 1–14, the target saturation rate was identical. The IDs 15 and 16 refer to simulations in which the process time was varied.

Two simulations were used as reference, where all parameters were chosen such that they were in the middle of the parametric ranges studied in this work. Unless specified otherwise, subsequent simulations use those default parameters. The default simulation without binder is denoted as ID 1 (cf. first column in Table 1). The default simulation with binder is denoted as ID 9.

Starting from ID 1, all influencing factors concerning the active material were studied independently. The parameters R_{PS} , ϕ_A , and θ_A we varied separately, while the other influencing factors were kept constant at their default values. The influence of the binder was studied by separately varying ϕ'_B or θ_B , while keeping all other influencing factors constant at the values identical to those from ID 1. The structural properties of the ID 15 and ID 16 were identical to those of ID 1.

Filling and permeability simulations were conducted for each ID. Numerical results are also given in Table 1.

Results and Discussion

Pressure-Saturation Behavior

Figure 2 shows the pressure-saturation curves of all simulations. They follow a sigmoidal behavior with steep sides for low and high saturations, and an almost horizontal regime for medium saturations. This trend can be explained by the Young-Laplace equation ($p_c = 2\gamma/R$) which describes the inverse proportionality between the capillary pressure p_c and the pore radius R . When electrolyte initially invades the electrode, smaller pores at the inlet need to get passed leading to an increase in Δp . Thereafter, a plateau is reached, during which the electrodes are primarily filled through larger pores. Finally, for high saturations, smaller pores have to be filled, leading to a strong increase in Δp again. For all cases, the final saturation S_{final}^E deviates from the theoretical optimum of 100% which is related to gas agglomerates being entrapped in the pore space.^[3,4,11,19,23,44,77,81,82]

Figure 2(a–d) shows the results for the influencing factors that are related to the active material and the process time. Figure 2(e and f) shows the results purely related to the binder. There and in all figures in the following, the influencing factors are indicated by the colors. The line types correspond to a specific value of the influencing factor. In Figure 2, the results of the reference cases ID 1 and ID 9 are depicted by the blue and purple solid lines, respectively.

Figure 2(a and b) shows the influence of the particle size distribution R_{PS} and the volume fraction ϕ_A of the active material. Compared to the reference, larger particle sizes (ID 3) and a smaller volume fraction of the active material (ID 5) result in a smaller Δp and an increased final saturation S_{final}^E . Both are

related to larger pores and reduced Δp . The contrary is observed for larger ϕ_A (ID 4) which facilitates gas entrapping.

The influence of the wetting behavior of active material is shown in Figure 2(c). The results indicate that decreasing θ_A or increasing the wettability reduces Δp and improves the saturation.

Figure 2(d) shows that there is hardly any influence of the process time t_p for the values studied here. The medium (ID 1) and slow (ID 15) filling processes were slow enough such that capillary forces dominated viscous forces. For a fast filling (ID 16), viscous effects are more apparent.^[77,83] The flow regime then tends to transition from capillary fingering to viscous fingering which leads to more gas entrapment.^[83,84]

Figure 2(e and f) shows the influence of the binder. In general, the binder shifted S_{init}^E to larger values. This was partially due to the definition of the saturation (cf. Eq. (2)), where adding a solid binder reduces the total pore space and was even more pronounced for strong wettabilities.

There is almost no influence of the inner volume fraction of the binder for the values studied here. This is different for the binder wettability. Using a strongly wetting binder (IDs 9–12) decreases Δp , enhances the electrolyte percolation, increases S_{init}^E , and improves the final saturation. In contrast, using a neutrally wetting (ID 13) or dewetting binder (ID 14) causes larger Δp . Moreover, a dewetting binder leads to effects similar to pore clogging. It prevents electrolyte invading the binder and entraps large amounts of residual gas in the binder and at its surface.

Total Duration of the Filling Process

The saturation-time behavior for different process times or target saturation rates is given in Figure S3 in the Supporting Information. The results show a similar qualitative behavior. The control function adjusts the inlet density increment such that a steady and uniform filling process is achieved. This is shown by the almost linear behavior of the saturation-time curves. Deviations from that behavior occur at the beginning and the end of the simulations, where Δp is highly sensitive to the saturation (cf. Figure 2).

As both a fast filling and a low final saturation decrease t_{end} , a relative measure, i.e. the reciprocal filling rate \tilde{t}_{end} , is introduced:

$$\tilde{t}_{end} = \frac{t_{end}}{S_{final}^E}. \quad (6)$$

It corresponds to the average time needed to fill 1% of electrode's pore space.

For the IDs 1–14, the results of t_{end} and \tilde{t}_{end} are shown in Figure 3. There is a clear correlation between t_{end} and the structural properties of the active material (IDs 1–5). The smaller the pores are, the shorter is the total duration. Moreover, there is a strong dependence between \tilde{t}_{end} and θ_A . Stronger wettabilities result in lower reciprocal filling rates and, thus, shorter filling processes. The same effect is observed for the binder wettability (IDs 9, 12–14) and has also been reported in

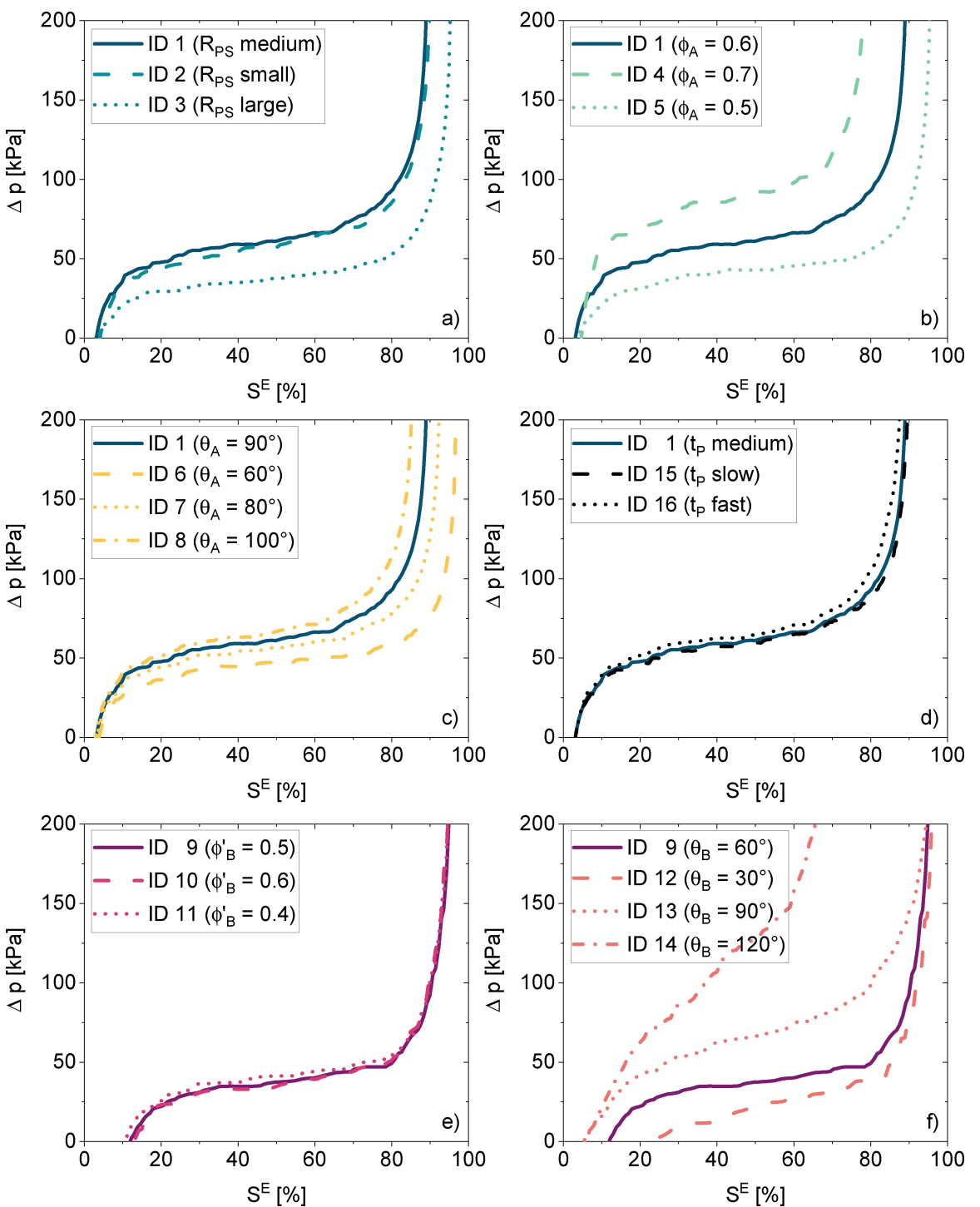


Figure 2. Pressure-saturation behavior of electrodes a)–d) without, and e)–f) with binder. ID 1 and ID 9 are depicted with the blue and purple solid lines, respectively. The influencing factors are indicated by the colors. Those are a) the particle size distribution R_{PS} (turquoise), b) the volume fraction of the active material ϕ_A (green), c) the wettability of the active material θ_A (orange), d) the process time t_p (black), e) the inner volume fraction of the binder ϕ'_B (magenta), and f) the wettability of the binder θ_B (red). The line types correspond to a specific value of the influencing factor.

the literature.^[12,41,85] In general, the filling of electrodes with binder is about 20% faster compared to electrodes without binder. However, this is also related to the reduction of the total pore space when adding binder.

Final Saturation and Gas Entrapment

First, the final saturations at the end of the filling process are compared. The numerical values of S_{final}^E are listed in Table 1 and shown in Figure 4.

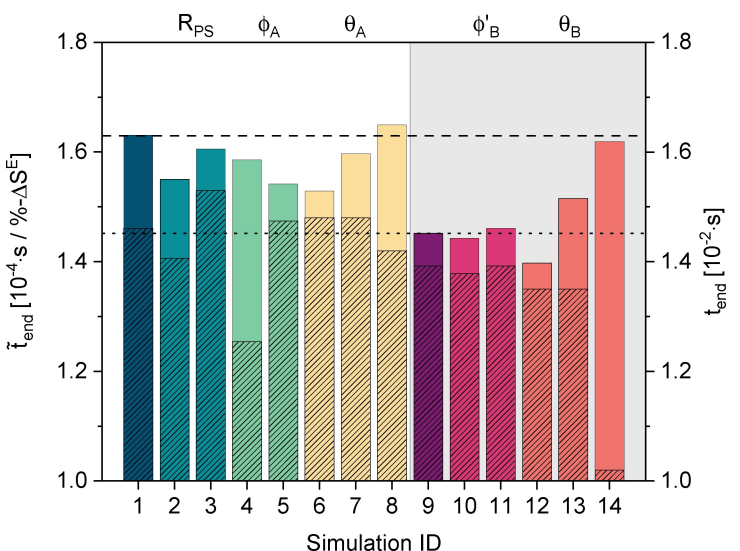


Figure 3. Overview of the reciprocal filling rate \tilde{t}_{end} and the total duration of the filling process t_{end} . The values of \tilde{t}_{end} are depicted with the colored bars and related to the left ordinate axis. The values of t_{end} are depicted with the hatched bars and related to the right ordinate axis. The influencing factors are indicated by the colors. The corresponding simulation IDs are given at the abscissa. Simulations of electrodes with binder are highlighted by the gray background. The horizontal dashed and dotted lines represent \tilde{t}_{end} of ID 1 and ID 9, respectively.

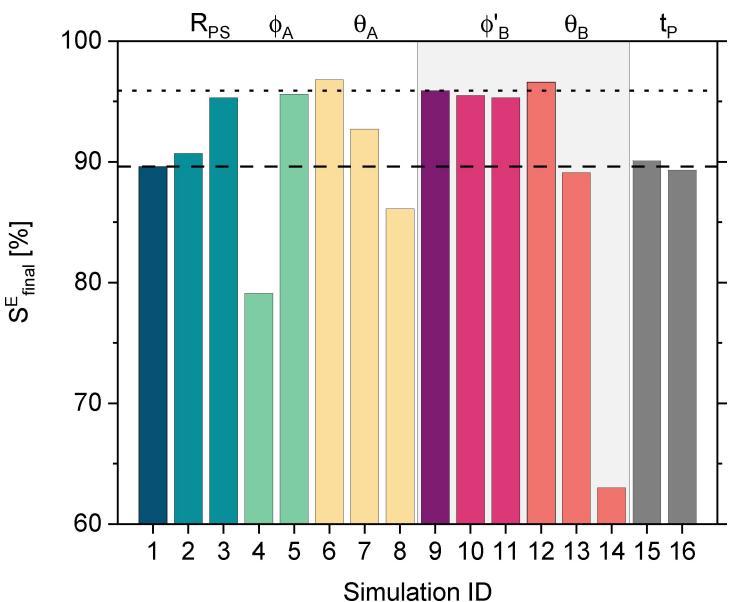


Figure 4. Overview of the final saturation of the filling process S_{final}^E . The meaning of the colors is identical to those from Figure 3. The horizontal dashed and dotted lines represent S_{final}^E of ID 1 and ID 9, respectively.

The final saturations are in a broad range $S_{\text{final}}^E = [63.0, 96.8]\%$ which corresponds to a residual gas volume fraction of $[37.0, 3.2]\%$. Most of the electrodes are filled 90% and more, which is in accordance with observations from experiments.^[4] Compared to ID 1 a larger saturation is observed for electrodes with 1) larger pores, i.e. larger R_{PS} (ID 3) or smaller ϕ_A (ID 5), 2) better wettability (IDs 6 and 7), and 3) in the presence of a hydrophilic binder (IDs 9–12). In contrast, incomplete filling correlates with 1) small pores (ID 4) and 2) hydrophobic active material (ID 8) and binder (ID 14). These general findings have been shown for single influencing factors

in experimental^[2,9,11–13,60] and simulative^[41,43–46,60,85] studies in the literature. Here, they are quantified and summarized for a broad variety of decoupled influencing factors. Together with the high spatial resolution of LBM in the sub-micrometer range and a detailed analysis, the results of the present work go far beyond the state-of-the-art knowledge and are further discussed in the following.

Figure 5 shows qualitative and quantitative information of the gas agglomerates for the two reference cases. The amount of residual gas phase is 10.4% in Figure 5(a) and 4.1% in Figure 5(b). In the top figure, the gas entrapment is shown

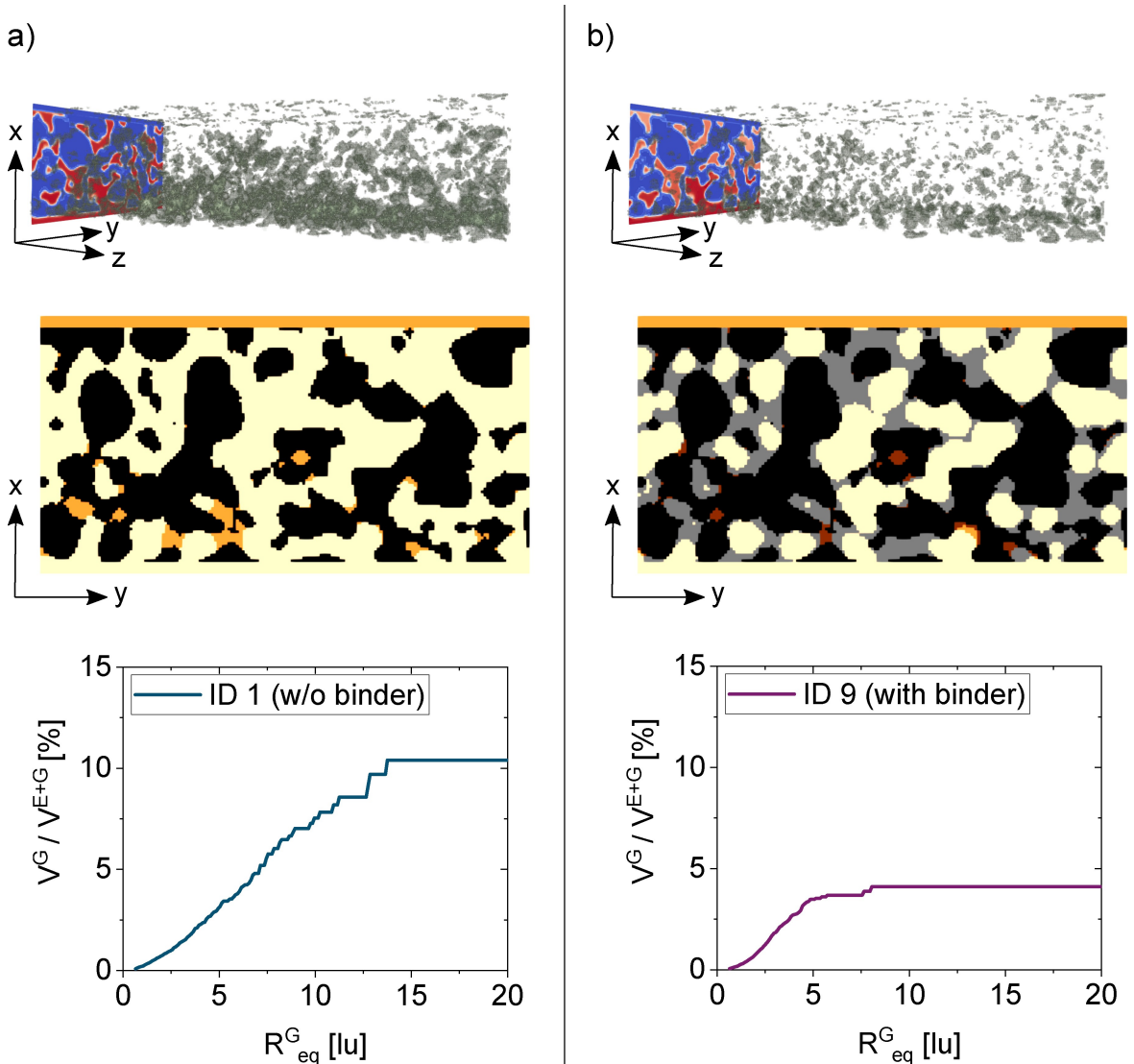


Figure 5. Comparison of the gas entrapment for the two reference simulations: a) ID 1 with 10.4 % residual gas phase and b) ID 9 with 4.1 % residual gas phase. Top: Visualization of the residual gas phase being entrapped in the electrodes at the end of the filling process. The gas phase is depicted in gray. The electrolyte and the solid components are fully transparent. Middle: Cross section through the xy-plane at $z = 200$ lu. The active material is depicted in black, the binder is depicted in gray, and the gas phase is depicted in red or orange in regions with or without binder, respectively. Bottom: Size distributions of gas agglomerates. The ratio of the cumulated gas volume V^G to the total pore volume V^{E+G} is shown as a function of the equivalent gas bubble radius R_{eq}^G .

qualitatively. There, gas agglomerates are depicted in gray. All other components are fully transparent. In the middle figure, a cross section through the xy -plane at $z = 200$ lu is shown, where active material, binder, and gas phase are depicted in black, gray, and red or orange in regions with or without binder, respectively. In the bottom figure, the size distributions of the gas agglomerates are given. They show the ratio of cumulated gas volume V^G to total pore volume V^{E+G} as a function of the equivalent gas bubble radius R_{eq}^G . Here, R_{eq}^G follows an IUPAC definition.^[86,87] It corresponds to the radius of a spherical gas bubble which has the equivalent volume as an irregularly shaped gas agglomerate observed in the pore space. The cumulated gas volume is the summed volume of all gas agglomerates from which the equivalent gas bubble radius is less or equal than R_{eq}^G .

The top row of Figure 5 shows that more gas phase and larger agglomerates are entrapped for ID 1, especially close to the inlet. This is also observed from the middle row of Figure 5 where most of the gas agglomerates are in the lower half of the figure. For ID 1, gas agglomerates are mainly entrapped in small pores and corners confined by active material. The location of gas agglomerates is similar to ID 9. However, since the binder has a better wettability than the active material gas agglomerates are smaller as is also shown in the quantitative plots at the bottom row of Figure 5.

The corresponding cross-sectional images and size distributions of all simulations are given in the Supporting Information (cf. Figures S4, S5 & S6). The most relevant findings of which are summarized in the following: 1) For almost all influencing factors, the slope $\Delta(V^G/V^{E+G})/\Delta R_{eq}^G$ is similar until the asymp-

totic end value of V^G/V^{E+G} is approached. This indicates a similar gas entrapment for small and medium gas agglomerates amongst all structures. 2) Larger volume fractions of active material and smaller pores lead to larger gas agglomerates and better connectivity of the gas phase. 3) A strong wettability of both active material and binder reduces gas entrapment and the size of gas agglomerates. 4) The process time slightly affects the size distribution of gas agglomerates. Applying a fast filling speed (ID 16) leads to the formation of more medium-sized gas agglomerates.

The residual gas phase with its low ionic conductivity, is known to have a twofold impact on the battery performance.^[3–6,11,44,69] Gas agglomerates inhibit the ion transport, leading to longer transport pathways, and thereby decreasing the effective ionic conductivity. In addition, gas prevents ion transport to the surface of the active material, reduces its electrochemically active surface area, increases overpotentials, and reduces the specific battery capacity.

The influence on the geodesic tortuosities as a measure for the effective conductivity is shown in Figure 6. Adding binder in general increases the tortuosity by approximately 10%.^[69] Moreover, τ_{end} behaves inversely proportional to S_{final}^E (cf. Figure 4). Thus, the transport pathways elongate when more gas agglomerates are entrapped. For most electrodes with $S_{\text{final}}^E > 90\%$ the influence is minor. However, in the extreme case (ID 14) the shortest pathway increases by 27.7%.

The influence of entrapped gas on the electrochemically active surface area $A_{\text{A,act}}$ is shown in Figure 7. As expected a direct proportionality of $A_{\text{A,act}}$ and S_{final}^E is observed. Better saturation and less residual gas phase decrease the surface area of active material being in contact with electrolyte. However, the quantities are surprising. Even for the best saturation (ID 6) and a strongly hydrophilic, i.e. gas repelling, surface, about 9%

of the total active surface area are passivated. For the worst case (ID 14) even 63.8% of active surface area are blocked.

Note that these results represent gas entrapment right after filling. It might differ from the gas entrapment at the end of the whole manufacturing process during which gas is either removed by evacuation or in subsequent production steps.

The aforementioned results (cf. Figures 6 and 7) confirm that electrode design and filling process have a huge effect on battery performance. As was shown previously in experiments^[11,14,18,69] and simulations,^[11,44] especially structural properties of the electrodes play an important role. The larger the pores are and the better they are connected, the better is the effective ionic conductivity and the more surface area remains electrochemically active. These effects can even be enhanced when increasing the wettability of electrode components. Thus, the results indicate, that increasing the power density by calendering electrodes increases the amount of entrapped gas which leads to a tortuosity increase and finally reduces battery capacity.

Permeability

The permeabilities of electrolyte and residual gas phase at the end of the filling process are shown in Figure 8. Numerical results are given in Table 1.

The general observations from Figure 8 are: 1) Permeabilities for electrodes without binder (IDs 1–8, 15, and 16) are about one order of magnitude larger than for cases with binder (IDs 9–14). 2) Gas permeabilities are mostly about one order of magnitude smaller than electrolyte permeabilities.

Both effects are mainly influenced by the solid-fluid interfacial contact area and the connectivity of the fluid

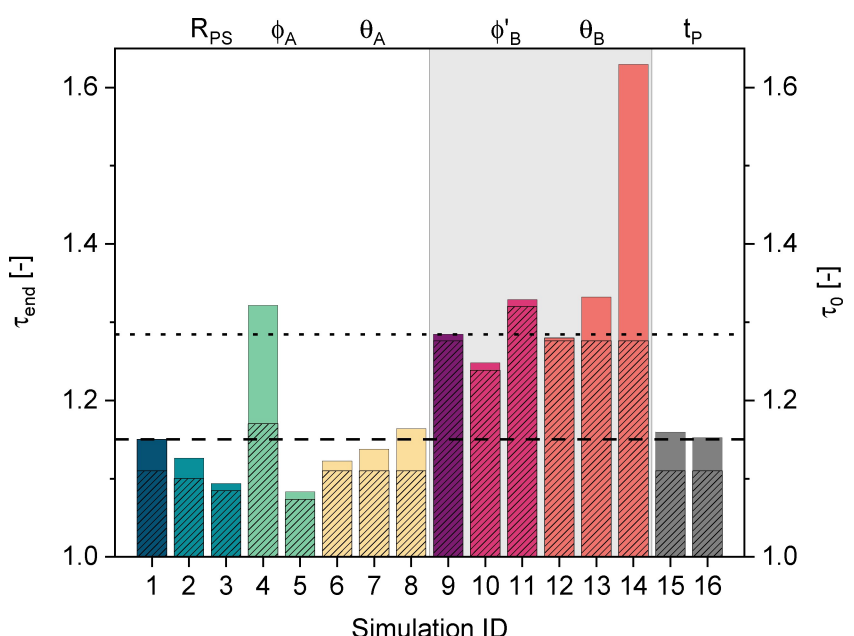


Figure 6. Overview of geodesic tortuosities τ_0 and τ_{end} . The values of τ_{end} are depicted with the colored bars and related to the left ordinate axis. The values of τ_0 are depicted with the hatched bars and related to the right ordinate axis. The meaning of the colors and line types is similar to those from Figure 3.

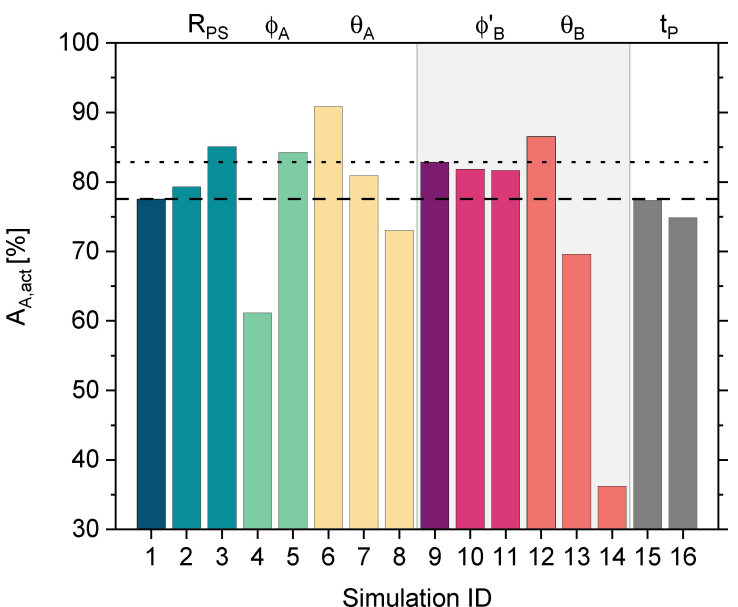


Figure 7. Overview of the ratio of the electrochemically active surface area $A_{A,active}$. The meaning of the colors is identical to those from Figure 3. The horizontal dashed and dotted line represent $A_{A,active}$ of ID 1 and ID 9, respectively.

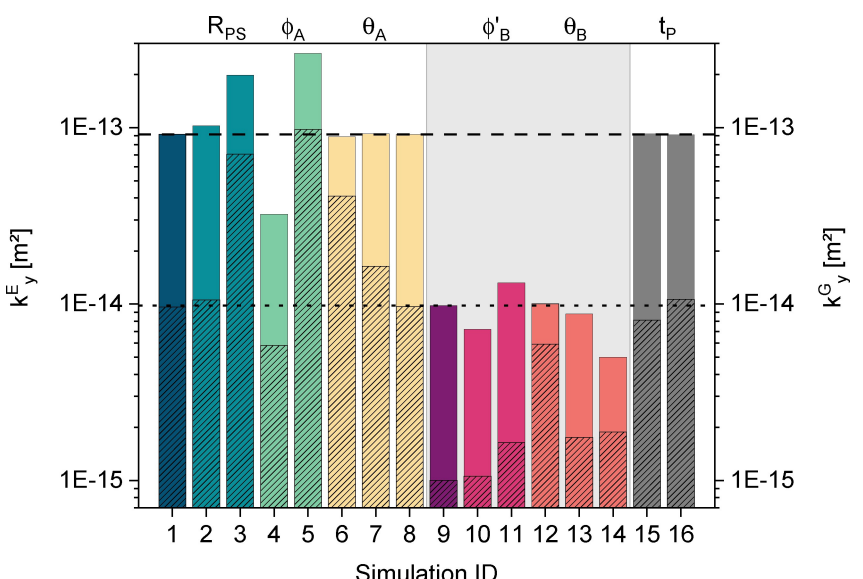


Figure 8. Overview of the electrolyte permeability k_y^E and the gas permeability k_y^G at the end of the filling process. The values of k_y^E are depicted with the colored bars and related to the left ordinate axis. The values of k_y^G are depicted with the hatched bars and related to the right ordinate axis. The meaning of the colors is identical to those from Figure 3. The horizontal dashed and dotted line represent k_y^E of ID 1 and ID 9, respectively.

phase.^[74] An increasing solid-fluid contact area increases the flow resistance, thus reducing the fluid mobility.^[74,75] In contrast, a better connectivity enhances the mobility.^[74,88] Electrodes without binder, and thus with less solid material, exhibit a smaller specific solid-fluid contact area, and lead to larger permeabilities. The residual gas phase, which has a remarkably smaller volume fraction than the electrolyte, has a low connectivity, and thus a lower permeability.

Beside the two aforementioned parameters, also structural properties,^[89–91] fluid saturation, wettability of the solids,^[74,75,89,92] and fluid-fluid interfacial area^[74,88,93] affect the permeability.

Apart from the fluid-fluid interfacial area, all other effects are shown in Figure 8 and are discussed in the following.

Large R_{PS} (ID 3) or small ϕ_A (ID 5) result in large values of k_y^E and k_y^G . In both cases the pores are comparable in size which leads to a small solid-fluid contact area and a low flow resistance.^[91] Moreover, the amount of residual gas phase and its connectivity is low for both structures (cf. Figure 4). Although, this typically decreases the permeability, here, the effect is dominated by drag of the electrolyte phase leading to large values of k_y^G , too. This has already been observed experimentally.^[88] It is also reproduced by the electrode

structures with binder (IDs 9–11) where the permeability increases for larger inner volume fractions.

An increasing wettability results from strong solid-fluid adhesion forces. Thus, the wetting phase is highly attracted by the solid, increases the solid-fluid interface, and decreases fluid mobility. This is different for the nonwetting phase.^[26,74] However, wettability and fluid connectivity are competing mechanisms that affect the permeability.^[74] While better wettability increases the flow resistance, an increased connectivity increases the fluid mobility. This is also shown in Figure 8 where the electrolyte permeability is hardly affected by the wettability of active material (IDs 1, 6–8). But when also taking into account the electrolyte saturation $S_{\text{final}}^{\text{E}}$ (cf. Figure 4) the link is not so clear anymore. As the contact angle θ_A increases, the saturation decreases and thereby reduces the electrolyte connectivity. Thus, an apparent effect is observed here. In fact, the enhanced electrolyte mobility for increasing contact angles is compensated by a decreased connectivity. This effect is even more pronounced for simulations in which the binder wettability was varied (IDs 9, 12–14). There, increasing θ_B counter-intuitively reduces the electrolyte permeability. The same two competing effects affect the gas phase. Thus, leading to an increased gas permeability for a better electrolyte wettability.

Conclusion

In this study, LBM simulations were used to improve the understanding of electrolyte filling processes on the pore scale. Therefore, a new lattice Boltzmann model for studying multiphase fluid flow simultaneously in pores of different length scales is presented. This model was applied to study electrolyte filling of realistic 3D lithium-ion cathodes with and without binder. Similarly other battery components as well as complete cells can be analyzed. The methodology is universal and can also be applied to other energy storage devices such as metal-air batteries, flow batteries or fuel cells. The influence of a wide range of relevant structural and physico-chemical properties as well as process parameters was studied. Large-scale simulations were conducted in which the particle size, volume fraction, and wettability of active material, the distribution, inner volume fraction, and wettability of binder, as well as the process time were varied. Pressure-saturation curves were determined. They show a systematic entrapment of residual gas that depends on the aforementioned parameters. A detailed analysis was conducted to understand the interdependencies of the amount, spatial distribution, and size of the gas agglomerates, as well as their effect on transport properties and electrochemically active surfaces.

In general, the findings indicate that the filling process is mainly influenced by structural electrode properties. It can be optimized by increasing the wettability. The influence of the process time is subordinate for the values studied here. At the end of the filling process, most electrodes contained 10% or less residual gas phase. It was shown that large pores with a narrow pore size distribution and hydrophilic active material

reduce gas entrapment. It could be further reduced when adding a wetting binder. Increasing the filling speed resulted in the entrapment of a slightly larger amount of medium-sized gas agglomerates. The worst saturation was observed for adding a dewetting binder.

A detailed analysis of the position and distribution of gas agglomerates was conducted and correlated with the battery performance. It was shown that gas agglomerates increase ionic transport pathways in electrodes and thus reduce the effective ionic conductivity. Moreover, gas agglomerates decrease the electrochemically active surface area. Both effects increase overpotentials during battery operation and have a negative impact on the specific battery capacity. The most favorable results were observed for electrodes with large pores, good pore space connectivity, and good wettability of electrode components. The results indicate that calendering electrodes could potentially reduce the power density of batteries.

Finally, it was shown which efforts are necessary to displace gas agglomerates from electrodes. For that, electrolyte and gas permeabilities at the end of the filling process were determined. The findings indicate that the binder decreases the mobility of gas agglomerates. The largest permeabilities were observed for large pores with a narrow pore size distribution and a wetting active material.

Altogether, it is shown that the new lattice Boltzmann model yields a detailed insight and a profound understanding of the influencing factors of filling processes on the pore scale. The results are promising and can especially be used to support electrode and electrolyte design as well as for optimizing the filling process.

Acknowledgement

The authors gratefully acknowledge financial support from the European Union's Horizon 2020 Research and Innovation Programme within the project "DEFACTO" [grant number 875247]. Furthermore, the presented work was financially supported by the Bundesministerium für Bildung und Forschung (BMBF) within the project HiStructures [grant number 03XP0243D]. The simulations were carried out on the Hawk at the High Performance Computing Center Stuttgart (HLRS) [grant LaBoRESys], and on JUSTUS 2 at the University Ulm [grant INST 40/467-1 FUGG]. Open Access funding enabled and organized by Projekt DEAL.

Conflict of Interest

The authors declare no conflict of interest.

Data Availability Statement

The data that support the findings of this study are available in the supplementary material of this article.

Keywords: gas entrapment • lattice Boltzmann method • lithium • microporous materials • multi-phase transport • two-phase flow

- [1] D. L. Wood, J. Li, C. Daniel, *J. Power Sources* **2015**, *275*, 234–242. doi:10.1016/j.jpowsour.2014.11.019.
- [2] J. B. Habedank, F. J. Günter, N. Billot, R. Gilles, T. Neuwirth, G. Reinhart, M. F. Zaeh, *The International Journal of Advanced Manufacturing Technology* **2019**, *102*, 2769–2778. doi:10.1007/s00170-019-03347-4.
- [3] T. Knoche, V. Zinth, M. Schulz, J. Schnell, R. Gilles, G. Reinhart, *J. Power Sources* **2016**, *331*, 267–276. doi:10.1016/j.jpowsour.2016.09.037.
- [4] W. Weydanz, H. Reisenweber, A. Gottschalk, M. Schulz, T. Knoche, G. Reinhart, M. Masuch, J. Franke, R. Gilles, *J. Power Sources* **2018**, *380*, 126–134. doi:10.1016/j.jpowsour.2018.01.081.
- [5] T. Knoche, F. Surek, G. Reinhart, *Procedia CIRP* **2016**, *41*, 405–410. doi:10.1016/j.procir.2015.12.044.
- [6] A. Schilling, S. Wiemers-Meyer, V. Winkler, S. Nowak, B. Hoppe, H. H. Heimes, K. Dröder, M. Winter, *Energy Technol.* **2020**, *8*, 1–7. doi:10.1002/ente.201900078.
- [7] M. Lanz, E. Lehmann, R. Imhof, I. Exnar, P. Novák, *J. Power Sources* **2001**, *101*, 177–181. doi:10.1016/S0378-7753(01)00706-6.
- [8] R. Imhof, P. Novák, *J. Electrochem. Soc.* **1998**, *145*, 1081–1087. doi:10.1149/1.1838420.
- [9] A. Schilling, P. Gümbel, M. Möller, F. Kalkan, F. Dietrich, K. Dröder, *J. Electrochem. Soc.* **2019**, *166*, A5163–A5167. doi:10.1149/2.0251903jes.
- [10] S. Müller, J. Eller, M. Ebner, C. Burns, J. Dahn, V. Wood, *J. Electrochem. Soc.* **2018**, *165*, A339–A344. doi:10.1149/2.0311802jes.
- [11] C. Sauter, R. Zahn, V. Wood, *J. Electrochem. Soc.* **2020**, *167*, 100546. doi:10.1149/1945-7111/ab9bfd.
- [12] M. S. Wu, T. L. Liao, Y. Y. Wang, C. C. Wan, *J. Appl. Electrochem.* **2004**, *34*, 797–805. doi:10.1023/B:JACH.0000035599.56679.15.
- [13] F. J. Günter, J. Keilhofer, C. Rauch, S. Rössler, M. Schulz, W. Braunwarth, R. Gilles, R. Daub, G. Reinhart, *J. Power Sources* **2022**, *517*, 230668. doi:10.1016/j.jpowsour.2021.230668.
- [14] A. Davoodabadi, J. Li, H. Zhou, D. L. Wood, T. J. Singler, C. Jin, *J. Energy Storage* **2019**, *26*, 101034. doi:10.1016/j.est.2019.101034.
- [15] S. S. Zhang, *J. Power Sources* **2006**, *162* (2 SPEC. ISS.) 1379–1394. doi:10.1016/j.jpowsour.2006.07.074.
- [16] M.-J. Kleefoot, S. Enderle, J. Sandherr, M. Bolsinger, T. Maischik, N. Simon, J. Martan, S. Ruck, V. Knoblauch, H. Riegel, *The International Journal of Advanced Manufacturing Technology* **2022**, *118*, 1987–1997. doi:10.1007/s00170-021-08004-3.
- [17] A. Davoodabadi, J. Li, Y. Liang, R. Wang, H. Zhou, D. Wood, T. J. Singler, C. Jin, *J. Electrochem. Soc.* **2018**, *165*, A2493–A2501. doi:10.1149/2.0341811jes.
- [18] A. Davoodabadi, C. Jin, D. L. Wood III, T. J. Singler, J. Li, *Extreme Mechanics Letters* **2020**, *40*, 100960. doi:10.1016/j.eml.2020.100960.
- [19] F. J. Günter, J. B. Habedank, D. Schreiner, T. Neuwirth, R. Gilles, G. Reinhart, *J. Electrochem. Soc.* **2018**, *165*, A3249–A3256. doi:10.1149/2.0081814jes.
- [20] S. Chen, G. D. Doolen, *Annu. Rev. Fluid Mech.* **1998**, *30*, 329–364. doi:10.1146/annurev.fluid.30.1.329.
- [21] T. Krueger, H. Kusumaatmaja, A. Kuzmin, O. Shardt, G. Silva, E. Viggen, *The Lattice Boltzmann Method: Principles and Practice*, Springer, 2016.
- [22] L. Chen, Q. Kang, Y. Mu, Y. L. He, W. Q. Tao, *Int. J. Heat Mass Transfer* **2014**, *76*, 210–236. doi:10.1016/j.ijheatmasstransfer.2014.04.032.
- [23] H. Liu, Q. Kang, C. R. Leonardi, S. Schmieschek, A. Narváez, B. D. Jones, J. R. Williams, A. J. Valocchi, J. Harting, *Comput. Geosci.* **2016**, *20*, 777–805. doi:10.1007/s10596-015-9542-3.
- [24] X. Shan, H. Chen, *Phys. Rev. E* **1993**, *47*, 1815–1819. doi:10.1103/PhysRevE.47.1815.
- [25] F. Diewald, M. P. Lautenschlaeger, S. Stephan, K. Langenbach, C. Kuhn, S. Seckler, H.-J. Bungartz, H. Hasse, R. Müller, *Computer Methods in Applied Mechanics and Engineering* **2020**, *361*, 112773. doi:10.1016/j.cma.2019.112773.
- [26] M. P. Lautenschlaeger, H. Hasse, *Mol. Phys.* **2020**, *118*, e1669838. doi:10.1080/00268976.2019.1669838.
- [27] S. Becker, H. M. Urbassek, M. Horsch, H. Hasse, *Langmuir* **2014**, *30*, 13606–13614. doi:10.1021/la503974z.
- [28] M. P. Lautenschlaeger, H. Hasse, *Fluid Phase Equilib.* **2019**, *482*, 38–47. doi:10.1016/j.fluid.2018.10.019.
- [29] M. P. Lautenschlaeger, H. Hasse, *Phys. Fluids* **2019**, *31*. doi:10.1063/1.5090489.
- [30] D. H. Jeon, H. Kim, *J. Power Sources* **2015**, *294*, 393–405. doi:10.1016/j.jpowsour.2015.06.080.
- [31] P. Satjaritanun, J. W. Weidner, S. Hirano, Z. Lu, Y. Khunatorn, S. Ogawa, S. E. Litster, A. D. Shum, I. V. Zenyuk, S. Shimparee, *J. Electrochem. Soc.* **2017**, *164*, E3359–E3371. doi:10.1149/2.0391711jes.
- [32] S. Sakaida, Y. Tabe, T. Chikahisa, *J. Power Sources* **2017**, *361*, 133–143. doi:10.1016/j.jpowsour.2017.06.054.
- [33] Z. Niu, Z. Bao, J. Wu, Y. Wang, K. Jiao, *Appl. Energy* **2018**, *232*, 443–450. doi:10.1016/j.apenergy.2018.09.209.
- [34] D. H. Jeon, *J. Power Sources* **2020**, *475*, 228578. doi:10.1016/j.jpowsour.2020.228578.
- [35] L. Zhu, H. Zhang, L. Xiao, A. Bazylak, X. Gao, P.-C. Sui, *J. Power Sources* **2021**, *496*, 229822. doi:10.1016/j.jpowsour.2021.229822.
- [36] J. B. Grunewald, N. Goswami, P. P. Mukherjee, T. F. Fuller, *J. Electrochem. Soc.* **2021**, *168*, 024521. doi:10.1149/1945-7111/abe5e8.
- [37] Z. Jiang, Z. Qu, *Energy Procedia* **2016**, *88*, 642–646. doi:10.1016/j.egypro.2016.06.091.
- [38] T. Danner, S. Eswara, V. P. Schulz, A. Latz, *J. Power Sources* **2016**, *324*, 646–656. doi:10.1016/j.jpowsour.2016.05.108.
- [39] Z. Y. Jiang, Z. G. Qu, L. Zhou, W. Q. Tao, *Appl. Energy* **2017**, *194*, 530–539. doi:10.1016/j.apenergy.2016.10.125.
- [40] Z. Y. Jiang, Z. G. Qu, L. Zhou, *Int. J. Heat Mass Transfer* **2018**, *123*, 500–513. doi:10.1016/j.ijheatmasstransfer.2018.03.004.
- [41] S. G. Lee, D. H. Jeon, B. M. Kim, J. H. Kang, C.-J. Kim, *J. Electrochem. Soc.* **2013**, *160*, H258–H265. doi:10.1149/2.017306jes.
- [42] S. G. Lee, D. H. Jeon, *J. Power Sources* **2014**, *265*, 363–369. doi:10.1016/j.jpowsour.2014.04.127.
- [43] D. H. Jeon, *Energy Storage Mater.* **2019**, *18*, 139–147. doi:10.1016/j.ensm.2019.01.002.
- [44] A. Shodiev, E. Primo, O. Arcelus, M. Chouchane, M. Osenberg, A. Hilger, I. Manke, J. Li, A. A. Franco, *Energy Storage Mater.* **2021**, *38*, 80–92. doi:10.1016/j.ensm.2021.02.029.
- [45] S. K. Mohammadian, Y. Zhang, *Int. J. Heat Mass Transfer* **2018**, *118*, 911–918. doi:10.1016/j.ijheatmasstransfer.2017.11.063.
- [46] A. Shodiev, M. Duquesnoy, O. Arcelus, M. Chouchane, J. Li, A. A. Franco, *J. Power Sources* **2021**, *511*, 230384. doi:10.1016/j.jpowsour.2021.230384.
- [47] G. G. Pereira, *Phys. Rev. E* **2016**, *93*, 1–14. doi:10.1103/PhysRevE.93.063301.
- [48] G. G. Pereira, *Applied Mathematical Modelling* **2017**, *44*, 160–174. doi:10.1016/j.apm.2016.11.009.
- [49] G. G. Pereira, *Applied Mathematical Modelling* **2019**, *75*, 481–493. doi:10.1016/j.apm.2019.05.050.
- [50] S. D. Walsh, H. Burwinkle, M. O. Saar, *Comput. Geosci.* **2009**, *35*, 1186–1193. doi:10.1016/j.cageo.2008.05.004.
- [51] D. Westhoff, I. Manke, V. Schmidt, *Comput. Mater. Sci.* **2018**, *151*, 53–64. doi:10.1016/j.commatsci.2018.04.060.
- [52] S. Hein, T. Danner, D. Westhoff, B. Prifling, R. Scurtu, L. Kremer, A. Hoffmann, A. Hilger, M. Osenberg, I. Manke, M. Wohlfahrt-Mehrens, V. Schmidt, A. Latz, *J. Electrochem. Soc.* **2020**, *167*, 013546. doi:10.1149/1945-7111/ab6b1d.
- [53] J. Latt, O. Malaspina, D. Kontaxakis, A. Parmigiani, D. Lagrava, F. Brogi, M. B. Belgacem, Y. Thorimbert, S. Leclaire, S. Li, F. Marson, J. Lemus, C. Kotsalos, R. Condradis, C. Coreixas, R. Petkantchin, F. Raynaud, J. Beny, B. Chopard, *Computers & Mathematics with Applications* **2021**, *81*, 334–350. doi:10.1016/j.camwa.2020.03.022.
- [54] J. Mosciński, M. Bargiel, Z. Rycerz, P. Jakobs, *Mol. Simul.* **1989**, *3*, 201–212. doi:10.1080/08927028908031373.
- [55] A. Bezrukov, M. Bargiel, D. Stoyan, *Part. Part. Syst. Charact.* **2002**, *19*, 111–118. doi:10.5566/ias.v20.p203-206.
- [56] J. Feinauer, A. Spettl, I. Manke, S. Strege, A. Kwade, A. Pott, V. Schmidt, *Mater. Charact.* **2015**, *106*, 123–133. doi:10.1016/j.matchar.2015.05.023.
- [57] J. Feinauer, T. Brereton, A. Spettl, M. Weber, I. Manke, V. Schmidt, *Comput. Mater. Sci.* **2015**, *109*, 137–146. doi:10.1016/j.commatsci.2015.06.025.
- [58] P. Soille, *Morphological Image Analysis: Principles and Applications*, 2nd Edition, Springer, New York, 2003. doi:10.1007/978-3-662-05088-0.
- [59] O. Falode, E. Manuel, *Journal of Petroleum Engineering* **2014**, *2014*, 1–12. doi:10.1155/2014/465418.
- [60] T. Akai, A. M. Alhammadi, M. J. Blunt, B. Bijeljic, *Transp. Porous Media* **2019**, *127*, 393–414. doi:10.1007/s11242-018-1198-8.
- [61] J. T. Gostick, M. A. Ioannidis, M. W. Fowler, M. D. Pritzker, *Electrochem. Commun.* **2008**, *10*, 1520–1523. doi:10.1016/j.elecom.2008.08.008.
- [62] I. R. Harkness, N. Hussain, L. Smith, J. D. Sharman, *J. Power Sources* **2009**, *193*, 122–129. doi:10.1016/j.jpowsour.2008.11.055.

- [63] J. D. Fairweather, P. Cheung, D. T. Schwartz, *J. Power Sources* **2010**, *195*, 787–793.
- [64] S. Dwenger, G. Eigenberger, U. Nieken, *Transp. Porous Media* **2012**, *91*, 281–294. doi: 10.1007/s11242-011-9844-4.
- [65] O. Stenzel, O. M. Pecho, L. Holzer, M. Neumann, V. Schmidt, *AIChE J.* **2016**, *62*, 1834–1843. doi:10.1002/aic.15160.
- [66] M. Neumann, O. Stenzel, F. Willot, L. Holzer, V. Schmidt, *Int. J. Solids Struct.* **2020**, *184*, 211–220. doi:10.1016/j.ijсолstr.2019.03.028.
- [67] D. Jungnickel, Graphs, Networks and Algorithms, 3rd Edition, Springer, Berlin, 2013. doi:10.1007/978-3-642-32278-5.
- [68] M. Neumann, C. Hirsch, J. Staněk, V. Beneš, V. Schmidt, *Scandinavian Journal of Statistics* **2019**, *46*, 848–884. doi:10.1111/sjos.12375.
- [69] M. Kroll, S. L. Karstens, M. Cronau, A. Höltzel, S. Schlabach, N. Nobel, C. Redenbach, B. Roling, U. Tallarek, *Batteries & Supercaps* **2021**, *4*, 1363–1373. doi:10.1002/batt.202100057.
- [70] D. A. G. Bruggeman, *Ann. Phys.* **1935**, *416*, 636–664. doi: 10.1002/andp.19354160705.
- [71] A. Vadakkepatt, B. Trembacki, S. R. Mathur, J. Y. Murthy, *J. Electrochem. Soc.* **2015**, *163*, A119–A130. doi:10.1149/2.0151602jes.
- [72] K. K. Patel, J. M. Paulsen, J. Desilvestro, *J. Power Sources* **2003**, *122*, 144–152. doi:10.1016/S0378-7753(03)00399-9.
- [73] K. Schladitz, J. Ohser, W. Nagel, Measuring intrinsic volumes in digital 3D images, in: A. Kuba, L. Nyúl, K. Palágyi (Eds.), 13th International Conference Discrete Geometry for Computer Imagery, Springer, 2007, pp. 247–258. doi:10.1007/11907350_21.
- [74] C. J. Landry, Z. T. Karpyn, O. Ayala, *Water Resour. Res.* **2014**, *50*, 3672–3689. doi:10.1002/2013WR015148.
- [75] H. Li, C. Pan, C. T. Miller, *Phys. Rev. E* **2005**, *72*, 1–14. doi:10.1103/PhysRevE.72.026705.
- [76] N. S. Martys, H. Chen, *Phys. Rev. E* **1996**, *53*, 743–750. doi:10.1103/PhysRevE.53.743.
- [77] Z. Li, S. Galindo-Torres, G. Yan, A. Scheuermann, L. Li, *Adv. Water Resour.* **2018**, *116*, 153–166. doi:10.1016/j.advwatres.2018.04.009.
- [78] Y. Sun, C. J. Radke, B. D. McCloskey, J. M. Prausnitz, *J. Colloid Interface Sci.* **2018**, *529*, 582–587. doi:10.1016/j.jcis.2018.06.044.
- [79] F. Wang, X. Li, *ACS Omega* **2018**, *3*, 6006–6012. doi:10.1021/acsomega.8b00808.
- [80] N. Rosman, W. Norharyati Wan Salleh, N. Asikin Awang, A. Fauzi Ismail, J. Jaafar, Z. Harun, *Materials Today: Proceedings* **2019**, *19*, 1413–1419. doi:10.1016/j.matpr.2019.11.162.
- [81] M. G. Schaap, M. L. Porter, B. S. Christensen, D. Wildenschild, *Water Resour. Res.* **2007**, *43*, 1–15. doi:10.1029/2006WR005730.
- [82] J. Avendaño, N. Lima, A. Quevedo, M. Carvalho, *Energies* **2019**, *12*, 664. doi:10.3390/en12040664.
- [83] H. Huang, J. J. Huang, X. Y. Lu, *Comput. Fluids* **2014**, *93*, 164–172. doi:10.1016/j.compfluid.2014.01.025.
- [84] R. Lenormand, E. Touboul, C. Zarcone, *J. Fluid Mech.* **1988**, *189*, 165–187. doi:10.1017/S0022112088000953.
- [85] F. G. Wolf, D. N. Siebert, R. Surmas, *Phys. Fluids* **2020**, *32*, 052008. doi:10.1063/5.0004681.
- [86] B. R. Jennings, K. Parslow, *Mathematical and Physical Sciences* **1988**, *419*, 137–149. doi:10.1098/rspa.1988.0100.
- [87] J. G. Calvert, *Pure Appl. Chem.* **1990**, *62*, 2167–2219. doi:10.1351/pac199062112167.
- [88] D. G. Avraam, A. C. Payatakes, *Transp. Porous Media* **1995**, *20*, 135–168. doi:10.1007/BF00616928.
- [89] Z. Dou, Z. F. Zhou, *Int. J. Heat Fluid Flow* **2013**, *42*, 23–32. doi:10.1016/j.ijheatfluidflow.2013.01.020.
- [90] D. Zhang, K. Papadakis, S. Gu, *Adv. Water Resour.* **2016**, *95*, 61–79. doi: 10.1016/j.advwatres.2015.12.015.
- [91] M. Ahkami, A. Parmigiani, P. R. Di Palma, M. O. Saar, X. Z. Kong, *Comput. Geosci.* **2020**, *24*, 1865–1882. doi:10.1007/s10596-019-09926-4.
- [92] A. Ghassemi, A. Pak, J. Pet. Sci. Eng. **2011**, *77*, 135–145. doi:10.1016/j.petrol.2011.02.007.
- [93] Z. Li, S. Galindo-Torres, G. Yan, A. Scheuermann, L. Li, *Transp. Porous Media* **2019**, *129*, 295–320. doi:10.1007/s11242-019-01288-w.

Manuscript received: February 25, 2022

Revised manuscript received: March 16, 2022

Accepted manuscript online: March 17, 2022

Version of record online: March 30, 2022